A Theoretical Model for Flow Boiling CHF From Short Concave Heaters

J. E. Galloway[1]

I. Mudawar
Professor and Director.

Boiling and Two-Phase Flow Laboratory,
School of Mechanical Engineering,
Purdue University,
West Lafayette, IN 47907

Experiments were performed to enable the development of a new theoretical model for the enhancement in CHF commonly observed with flow boiling on concave heaters as compared to straight heaters. High-speed video imaging and photomicrography were employed to capture the trigger mechanism for CHF for each type of heater. A wavy vapor layer was observed to engulf the heater surface in each case, permitting liquid access to the surface only in regions where depressions (troughs) in the liquid–vapor interface made contact with the surface. CHF in each case occurred when the pressure force exerted upon the wavy vapor–liquid interface in the contact regions could no longer overcome the momentum of the vapor produced in these regions. Shorter interfacial wavelengths with greater curvature were measured on the curved heater than on the straight heater, promoting a greater pressure force on the wavy interface and a corresponding increase in CHF for the curved heater. A theoretical CHF model is developed from these observations, based upon a new theory for hydrodynamic instability along a curved interface. CHF data are predicted with good accuracy for both heaters.

1 Introduction

It is well known that CHF in pool boiling can be ameliorated by increasing the magnitude of body force normal to the heater surface as suggested, for example, by the well-known CHF model of Zuber et al. (1961). Costello and Adams (1963), Marto and Gray (1971), and Usenko and Fainzil'berg (1974) all demonstrated this CHF enhancing effect by rotating the heater and liquid as a solid body. Gambill and Green (1958), Miropol'skiy and Pikus (1969), Hughes and Olson (1975), Iverson and Whitaker (1988), and Gu et al. (1989) proposed more practical means of creating an "effective" body force by supplying subcooled liquid over concave heated surfaces. Today, many heat sinking devices can be found in the aerospace industry that are grooved to accommodate closely spaced serpentine coolant channels in order to increase both CHF and the channel wetted area relative to the device surface area subjected to the heating. It has been postulated by most of the above-cited authors that flow over curved surfaces produces a centrifugal force that facilitates the removal of vapor from the heated surface, thus increasing CHF relative to a straight surface. This effect was accounted for using pool boiling CHF correlations or models that were modified by replacing Earth gravity with centrifugal acceleration.

Curved flow boiling experiments were conducted by the authors of the present study using a stirred cylindrical vessel facility (Galloway and Mudawar, 1989, 1992). Heat sources were flush-mounted to the inner wall of a cylindrical vessel partially filled with liquid. Flow with streamwise curvature was created by rotating a radial-bladed stirrer along the axis of the vessel creating an annular liquid layer as shown in Fig. 1. Photographs were recently taken in a sideview orientation relative to the streamwise direction by a boroscope lens. While accurate measurements of interfacial features were extremely difficult, this new photographic study clearly revealed the formation of a

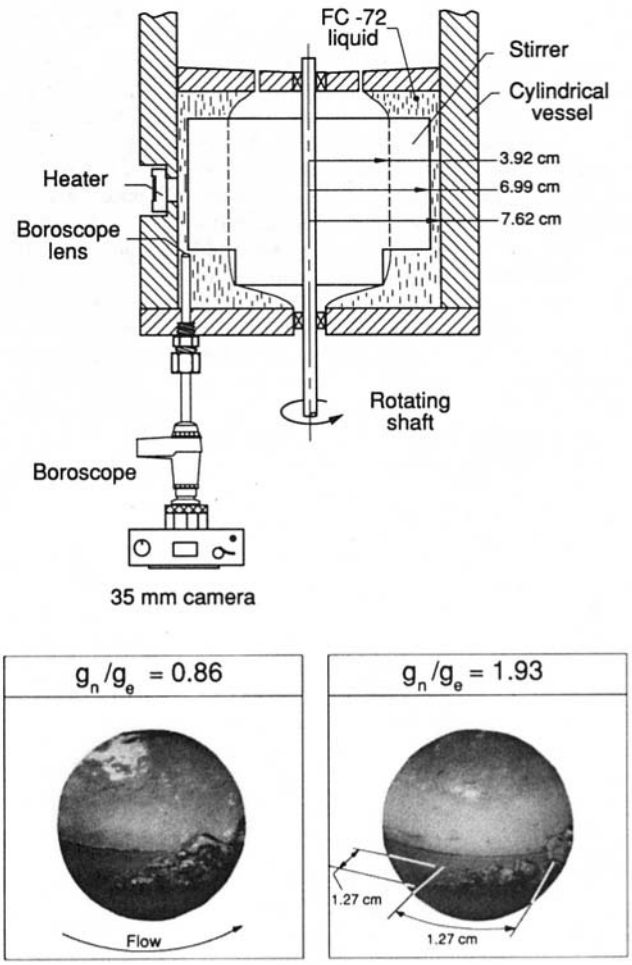

Fig. 1 Stirred vessel boroscope system and photographs of the wavy vapor layer at 99 percent of CHF

[1] Present address: Advanced Manufacturing Technology, Radio Products Group, Motorola, Fort Lauderdale, FL 33322.

Contributed by the Heat Transfer Division for publication in the JOURNAL OF HEAT TRANSFER. Manuscript received by the Heat Transfer Division January 1994; revision received November 1994. Keywords: Augmentation and Enhancement, Boiling, Flow Instability. Associate Technical Editor: V. K. Dhir.

wavy vapor layer at fluxes nearing CHF with nucleate boiling partially persisting beneath the vapor layer. The wavelength of vapor layer decreased with increasing angular velocity.

The objectives of the present study are to explore the mechanisms governing the effects of surface curvature on flow boiling CHF from short heaters, using an apparatus that lends itself better to high-resolution photographic study of interfacial features, and develop a theoretical model for this important flow configuration. These objectives are accomplished by comparing both CHF data and photographic records of vapor production at CHF for a concave heater to that for a straight heater. Relevant mechanisms for CHF on straight heaters will be reviewed first to establish a basis for this comparative study.

2 CHF From Straight Heaters

Interfacial Separation CHF Model. In a recent study, the authors examined near-wall interfacial behavior at CHF from a 12.7 mm long straight heater in vertical upflow using Fluorinert FC-87 (Galloway and Mudawar, 1993a, b). A wavy vapor layer similar to that depicted in Fig. 1 for the stirred vessel was observed over the straight heater as well as illustrated in Fig. 2. At heat fluxes nearing CHF, liquid contact with the heater surface was possible over the most upstream portion of the heater ($0 < z < z^*$) and within *wetting fronts*, corresponding to the wave troughs, while regions between the wetting fronts were dry. Heat could only be transferred within the isolated wetting fronts with a local heat flux many times greater than the average surface heat flux. At CHF, intense vapor production caused separation of the vapor layer interface from the heated surface starting at the location of the most upstream wetting front. This upstream separation increased heat flux in the downstream wetting fronts that lifted off the surface, in succession, until the entire interface separated from the surface, except for the most upstream region of the heater.

Statistical analysis of a large data base of interfacial features revealed the wetting fronts were separated by wavelengths twice the critical Helmholtz wavelength, λ_c, based upon hydrodynamic conditions at z^*. High-speed video imaging showed that only every other wave trough was able to create a wetting front at z^*. Once a wetting front was formed, a thin layer of liquid was splashed upon the surface and the ensuing intense vapor production pushed the next wave trough away from the surface, preventing the formation of a wetting front. Rapid dryout of this liquid cleared the surface for liquid replenishment with the advent of the third wave trough, thus allowing the formation of a new wetting front. This process, therefore, enabled the interfacial waves to produce wave fronts separated by wavelengths equal to $2\lambda_c$.

The data base for the straight heater also revealed that the span (length) of each wetting front was one-fourth the separation distance between wetting fronts. A surface energy balance yielded the following expression for CHF:

$$q_m = \left[1 - \frac{\lambda_c}{16(L - z^*)}\right]\frac{q_l}{4} \tag{1}$$

where the coefficient in the brackets is close to unity (i.e., CHF is about one-fourth the heat flux concentrated in the wetting fronts) for most operating conditions and accounts for continuous wetting in the region $0 < z < z^*$ and any partial wetting fronts in the downstream region, and q_l is the heat flux required to cause lifting of the most upstream wetting front. This lift-off heat flux was assumed to occur when the normal momentum of vapor generated in the wetting front just exceeds the pressure force exerted upon the interface as a result of interfacial curvature.

$$\rho_g\left[\frac{q_l}{\rho_g h_{fg}\left(1 + \frac{c_{p,f}\Delta T_{sub}}{h_{fg}}\right)}\right]^2 = \overline{P_f - P_g}, \tag{2}$$

Nomenclature

a_1, a_2 = coefficients in Eq. (12a)
A_f = coefficient in the liquid mean velocity profile
A_g = coefficient in the vapor mean velocity profile
b_1, b_2 = coefficients in Eq. (12b)
c = wave speed
c_i = imaginary component of wave speed
c_p = specific heat at constant pressure
c_r = real component of wave speed
D_h = hydraulic diameter
f = friction factor
F = amplitude function defined in Eq. (10a)
G = amplitude function defined in Eq. (10b)
g_e = Earth gravity
g_n = component of body force per unit mass normal to liquid–vapor interface
H = channel height = $H_f + H_g$, $R_2 - R_1$
H_f = liquid layer thickness
H_g = vapor layer thickness
h_{fg} = latent heat of vaporization
k = wave number = $2\pi/\lambda$
k_c = critical wave number = $2\pi/\lambda_c$
L = heater length
n = number of wetting fronts
P = pressure
$\overline{P_f - P_g}$ = mean interfacial pressure difference in wetting front $= \frac{1}{0.25\lambda}\left[\int_{3\lambda/8}^{5\lambda/8}(P_f - P_g) \times \frac{2\pi}{\lambda}\, d(\theta R_0 - c_r t)\right]$
ΔP = streamwise pressure drop
q = heat flux (electrical power divided by heater surface area)
q_l = heat flux (at CHF) corresponding to wetting front separation
q_m = critical heat flux (CHF)
r = radial coordinate
R_0 = radius of unperturbed interface
R_1 = inner radius of curved channel
R_2 = outer radius of curved channel
Re = Reynolds number = $\bar{u}_m D_h/\nu$
s = channel thickness normal to viewing axis
t = time
ΔT_{sub} = inlet liquid subcooling
u = phase velocity in the θ direction
u' = fluctuating component of u
$\bar{u}$ = mean component of u
$\bar{u}_i$ = interfacial value of $\bar{u}$
$\bar{u}_m$ = mean of $\bar{u}$ across liquid or vapor layer
U_m = mean liquid velocity upstream of heater
v = phase velocity in the r direction
v' = fluctuating component of v
z = spatial coordinate in the streamwise direction = $R_2\theta$
z^* = distance from leading edge of heater to center of first wetting front = $z_0 + \lambda_c(z^*)$
z_0 = position from leading edge where $\bar{u}_{g,i} - \bar{u}_{f,i} = 0$
δ = mean vapor layer thickness = H_g
η = interfacial displacement
θ = circumferential coordinate
λ = wavelength of interfacial perturbation
λ_c = critical wavelength corresponding to onset of instability
ν = kinematic viscosity
ρ = density
ρ'' = modified density defined in Eq. (3)
ρ''' = modified density defined in Eqs. (18a) and (18b)
σ = surface tension
τ = wetting period
τ_f = wall shear stress in the liquid layer

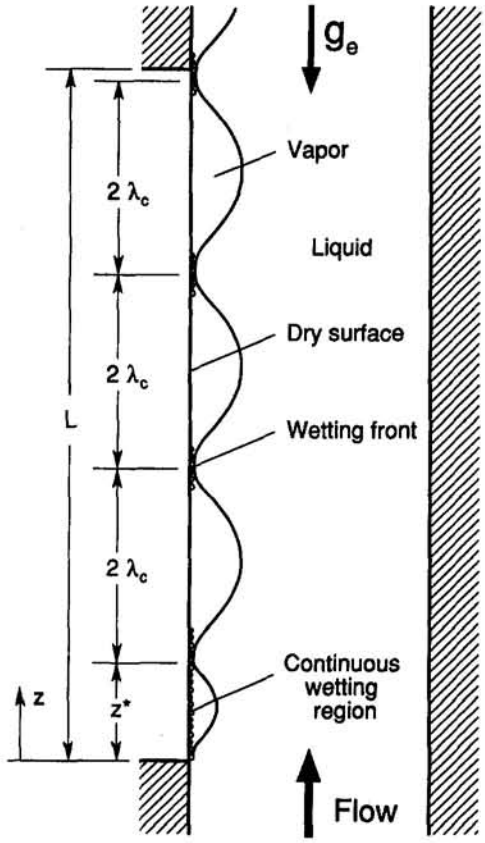

Fig. 2 Wetting front propagation along a straight heater at 99 percent of CHF (adapted from Galloway and Mudawar, 1993b)

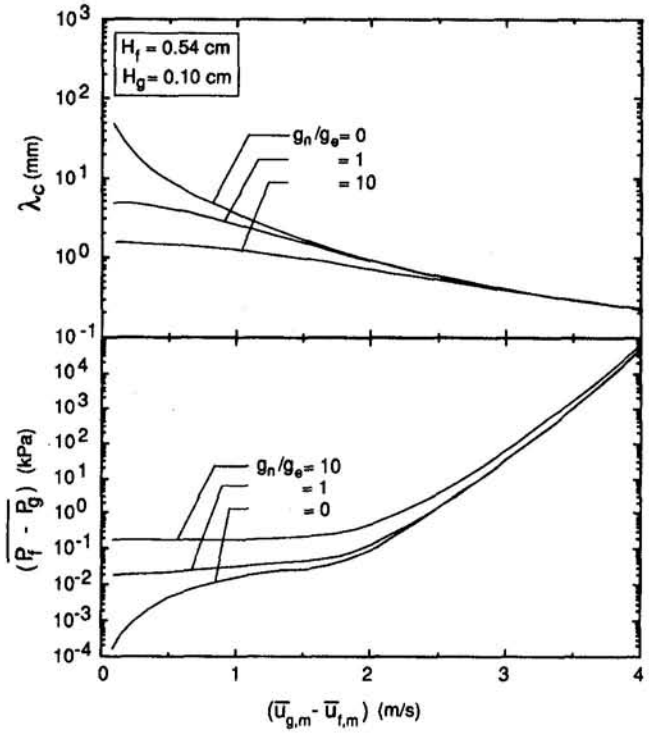

Fig. 3 Predictions of critical wavelength and interfacial pressure difference based on simplified instability theory for different values of velocity difference and body force

where the average pressure difference across the interface, $\overline{P_f - P_g}$, was calculated by integrating the pressure difference over the span of the most upstream wetting front.

Interfacial Instability Over Straight Heaters. The interfacial waviness illustrated in Fig. 2 can be idealized as a hydrodynamic instability of an interface between a vapor layer of mean velocity $\overline{u}_{g,m}$ and height H_g and a liquid layer of mean velocity $\overline{u}_{f,m}$ and height H_f. Using classical instability theory, the interfacial pressure difference resulting from a sinusoidal perturbation η perpendicular to the unperturbed interface can be expressed as (Galloway and Mudawar, 1993b)

$$P_f - P_g = -\eta k[\rho_f''(c - \overline{u}_{f,m})^2 + \rho_g''(\overline{u}_{g,m} - c)^2] - (\rho_f - \rho_g)g_n\eta = -\sigma k^2\eta, \quad (3)$$

where $\rho_f'' = \rho_f \coth(kH_f)$, $\rho_g'' = \rho_g \coth(kH_g)$, and g_n is the body force per unit mass perpendicular to the unperturbed interface ($g_n = 0$ for vertical upflow over a straight heater).

The critical wavelength for a straight channel is given by (Galloway and Mudawar, 1993b)

$$\frac{2\pi}{\lambda_c} = k_c = \frac{\rho_f''\rho_g''(\overline{u}_{g,m} - \overline{u}_{f,m})^2}{2\sigma(\rho_f'' + \rho_g'')} + \sqrt{\left[\frac{\rho_f''\rho_g''(\overline{u}_{g,m} - \overline{u}_{f,m})^2}{2\sigma(\rho_f'' + \rho_g'')}\right]^2 + \frac{g_n(\rho_f - \rho_g)}{\sigma}}. \quad (4)$$

An approximate method to account for the effect of flow curvature on CHF is to define an effective centrifugal force perpendicular to the heater surface based on the mean inlet liquid velocity and the heater radius of curvature, $g_n = U_m^2/R_2$. The effective centrifugal force per unit mass for the conditions of the present study varied from 0.3 to $9.7g_e$ corresponding to flow velocities between 0.35 and 2.0 m/s and a 4.19-cm heater radius of curvature.

Shorter wavelengths increase curvature, allowing the surface tension force to overcome the destabilizing effects of the body force and inertia. However, as the wavelength exceeds λ_c, the surface tension force no longer can maintain stability. Figure 3 shows the destabilizing effects of inertia and body force on the critical wavelength for the operating conditions of the present study as predicted by Eq. (4). The critical wavelength decreases rapidly with increasing velocity difference, $(\overline{u}_{g,m} - \overline{u}_{f,m})$, in the absence of a body force. However, as g_n increases above $10\,g_e$, the critical wavelength becomes relatively insensitive to inertia for velocity differences below 1 m/s. As the velocity difference exceeds 2.0 m/s, the critical wavelength becomes controlled primarily by inertia, insensitive to the magnitude of body force for the range of g_n shown.

Nomenclature (cont.)

τ_g = wall shear stress in the vapor layer
τ_i = interfacial shear stress
ϕ = potential function

Subscripts

f = saturated liquid
g = saturated vapor
i = interface
m = mean
sub = subcooling

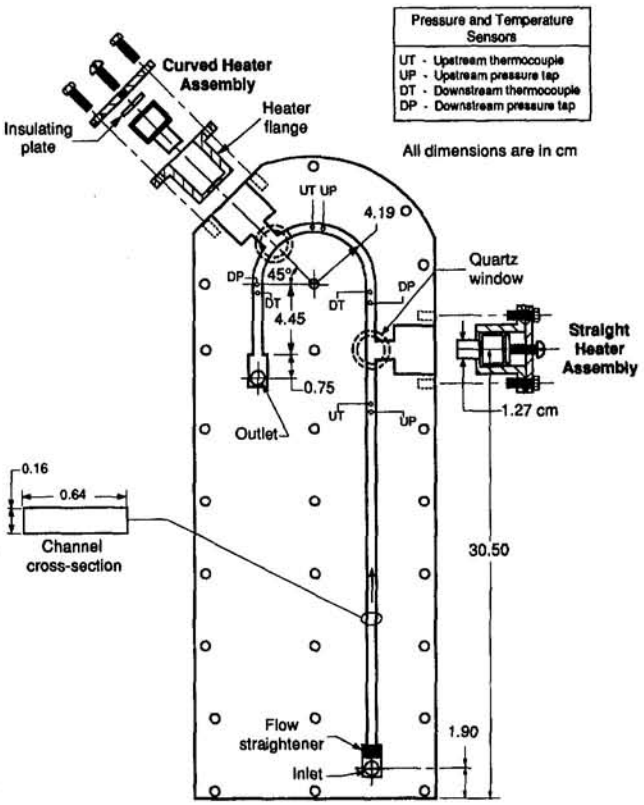

Fig. 4 Planar view of flow channel module

Figure 3 also shows, according to Eq. (3), pressure difference across the liquid–vapor interface, $P_f - P_g$, increases with increasing $(\bar{u}_{g,in} - \bar{u}_{f,in})$. An increase in the body force also produces a greater pressure force against the interface, which enables the interface to sustain a greater vapor momentum, or heat flux, before the interface can be separated from the heater surface. Therefore, increases in body force enhance CHF.

While this analysis clearly suggests that a greater body force would increase CHF, using an effective body force proportional to U_m^2/R_2 is, at best, a rough approximation of the net radial force resulting from the flow curvature. The excess force exerted upon the vapor–liquid interface for a curved heater compared to a straight heater is the result of radial pressure forces, which are dependent upon the channel geometry and the mean thickness and mean velocity of both the vapor and liquid layers. Additionally, the instability relations developed for a straight channel, Eqs. (3) and (4), simply do not apply for curved channels; hence the need for a new instability model applicable to a curved interface. Such a model will be presented later in this paper.

3 Experimental Methods

The curved flow apparatus was carefully designed to maximize photographic access to the heater surface. The apparatus consisted of a curved flow channel having a 4.19-cm outer radius of curvature, which was located downstream from a straight channel. A 1.27-cm-long heater was inserted in each of the straight and curved regions of the channel. As shown in Fig. 4, the flow channel was formed by milling a 0.16 cm × 0.64 cm slot in a Lexan plate. A second Lexan plate was clamped onto the first plate trapping an O-ring seal. Fully developed flow was established upstream of the straight heater by using an entrance length of over 100 times the hydraulic diameter. The centerline of the curved heater was positioned at a 135-deg angle relative to the inlet flow. Each of the straight and curved heaters was constructed from a copper block inserted inside an insulating flange made from G-10 insulating fiberglass. An O-ring was pressed between the base of each heater assembly and the flow channel plate providing a leak proof seal. Maximum errors of 8 percent and ±0.2°C were estimated in the measurement of heat flux and surface temperature, respectively, due to the uncertainty associated with thermocouple placement and calibration. Additional details concerning the flow loop and heater design can be found elsewhere (Galloway and Mudawar, 1993a).

FC-87, a 3M dielectric fluid, was tested at a pressure of 1.37 bars (T_{sat} = 39°C) with 8°C inlet subcooling. The relevant properties of FC-87 at these conditions are: $\rho_f = 1742$ kg/m^3, $\rho_g = 16.8$ kg/m^3, $\nu_f = 2.57 \times 10^{-7}$ m^2/s, $\nu_g = 7.15 \times 10^{-7}$ m^2/s, $c_{p,f} = 1099$ J/kg·K, $h_{fg} = 85{,}500$ J/kg, and $\sigma = 10.9 \times 10^{-3}$ N/m. By tilting the entire flow channel module, all tests were conducted in an upflow configuration with respect to the tested heater; only one heater was operated at a time.

At approximately 85 percent of CHF, a decrease in the slope of the heat flux versus wall superheat curve (detailed boiling curves can be found in Galloway, 1991) signaled the approach of CHF and was used as an indicator to reduce the increments in heater power to values no greater than 0.5 W/cm^2, each time waiting for the surface temperature to assume a new steady-state value before any additional power was supplied. CHF typically commenced from a stable surface temperature of approximately 85°C.

4 Experimental Results

Observations. At a heat flux of about 85 percent of CHF, large coalescent bubbles were observed sliding over the heater surface for both the straight and curved heaters. The length of these coalescent bubbles increased with increasing heat flux until, eventually, a fairly continuous wavy vapor layer was formed over the heater surface at heat fluxes below CHF. Boiling was sustained by liquid entrainment in the heater most upstream region and in the wetting fronts, where the liquid–vapor interface made contact with the heater surface. Experimental evidence supporting this wetting front description is also available from studies by Fiori and Bergles (1970), Hino and Ueda (1985a, b), and Galloway and Mudawar (1992), all of whom measured fluctuations in the heater surface temperature synchronous with the passage of vapor slugs.

The wavy vapor layer is depicted for the curved heater in Fig. 5 corresponding to heat fluxes equal to 99 percent of CHF. Boiling curves over the entire heat flux range leading to CHF proved the conditions depicted in Fig. 5 correspond to the nucleate boiling and not transition or film boiling regimes (Galloway, 1991). Using a magnification better than 50×, no vapor jets could be seen emanating from the heater surface. Rather, a violent surge of small bubbles in the wetting fronts was observed to be feeding the vapor layer. Like the stirred vessel described earlier and the straight heater, the wavelength for the curved heater decreased with increasing velocity. Excluding velocities above 1.25 m/s, the interfacial instability was clearly two dimensional, precluding any significant secondary flow effects. In fact, recent tests with heaters much wider than the one employed in the present study proved this instability is indeed two dimensional, both over straight heaters (Gersey and Mudawar, 1994) and curved heaters (Galloway, 1991).

However, the curved heater exhibited significant differences in the shape of the wavy vapor layer as compared to the straight heater. For equal inlet velocities, the interfacial wavelength was greater for the straight heater than for the curved heater and, occasionally, the curved heater projected vapor away from its surface in the form of vapor slugs, which protruded from the wave peaks at inlet velocities exceeding approximately 1.25 m/s. No such behavior was observed with the straight heater.

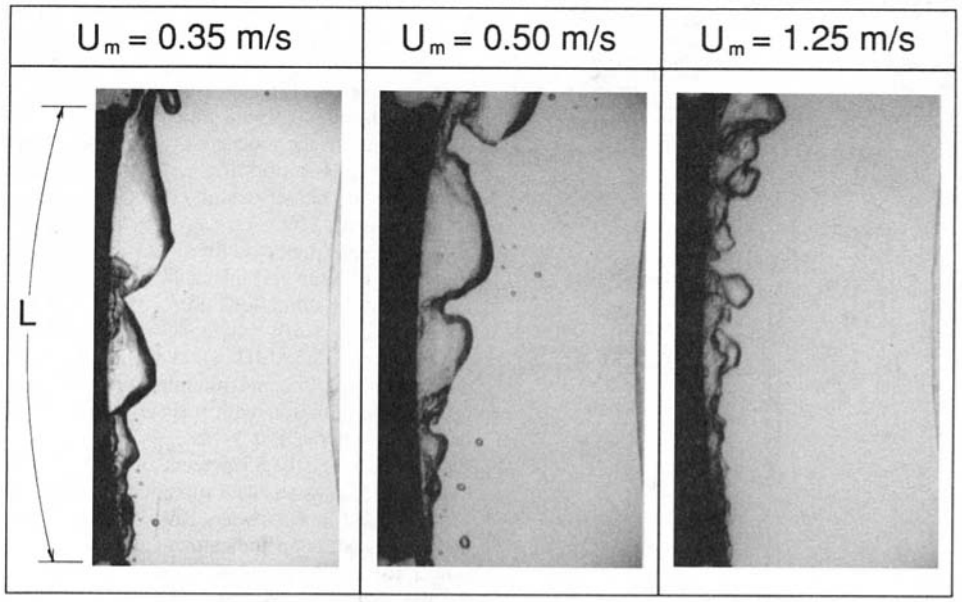

Fig. 5 Curved heater interfacial waves at 99 percent of CHF

Vapor Layer Interfacial Features. Vapor layer mean thickness and wavelength were measured from high-speed video images captured by a 6000 partial frames per second EktaPro 1000 motion analyzer, which were later analyzed on a 55-cm-wide screen. A measurement accuracy of ±0.1 mm was estimated from the combined magnification of the optical hardware and video screen. Thirty measurements were made for each inlet velocity to quantify the randomness of the interfacial features. Figure 6 shows that the wavelength for the straight heater was greater than for the curved heater and the wavelengths for both heaters decreased with increasing inlet velocity. Figure 6 also compares the ratio of wavelength to mean thickness of the vapor layer for both heaters. It should be emphasized that for each value of mean velocity in Fig. 6 a different CHF value was obtained for the curved channel as compared to the straight channel, differences in CHF for each velocity are discussed later (see Fig. 9). Vapor layer thickness was measured as half the normal distance between the surface and vapor layer interface after truncating the vapor projected from the wave peaks. Because vapor slugs perturbed the interface, particularly at velocities above 1.25 m/s, the curved heater thickness measurements tended to underestimate the vapor production for these high velocities. For a sinusoidal wave with wavelength λ and amplitude η_0, curvature at the wave peak is proportional to $(\eta_0/\lambda)^2/\eta_0$. Since the straight and curved heaters produced waves with fairly equal amplitudes, Fig. 6 indicates the waves acquired greater curvature over the curved heater than they did over the straight heater. This increased curvature increases the pressure force exerted upon the interface and, consequently, increases both the lift-off heat flux in the wetting fronts and CHF relative to the straight heater. The curved heater produced an average of 23 percent enhancement in CHF, compared to the straight heater, as shall be seen in the next section.

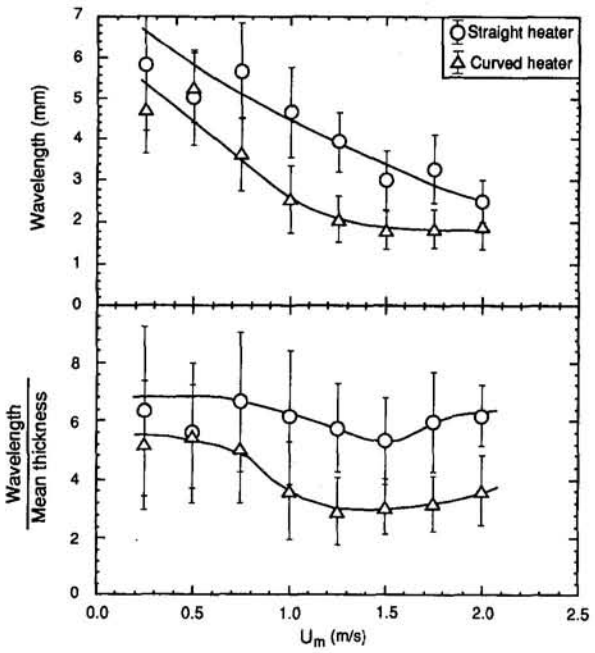

Fig. 6 Vapor layer wavelength and ratio of wavelength to mean thickness at 99 percent of CHF and z/L = 2/3

5 CHF Model

The model presented here is built upon physical observations, which are based on extensive high-speed video imaging studies, as discussed in the previous section, and are illustrated in Fig. 7: (1) at heat fluxes approaching CHF, vapor coalesces to form a fairly continuous wavy vapor layer; (2) liquid is entrained at wetting fronts where the liquid–vapor interface makes contact with the heater surface; (3) vigorous boiling persists near the leading edge of the heater and in the wetting fronts while regions between neighboring wetting fronts dry out; (4) CHF commences when the liquid–vapor interface separates from the heater surface at the location of the most upstream wetting front; and (5) remaining wetting fronts are separated, in succession, after separation of the upstream wetting front.

As shown in Fig. 7, the first wetting front is established at a distance z^* from the leading edge and then propagates along the heater surface at a speed c_r. The vapor layer interfacial wavelength, $2\lambda_c$, was determined from a new hydrodynamic instability model (discussed in the next section) and observations made using the high-speed video imaging. When the liquid–vapor interface is unstable, a disturbance having a wavelength equal to λ_c is assumed to touch the heater surface at $z = z^*$ (z^* is slightly greater than λ_c, the difference being a negligible distance z_0 over which the vapor velocity just exceeds the liquid velocity as

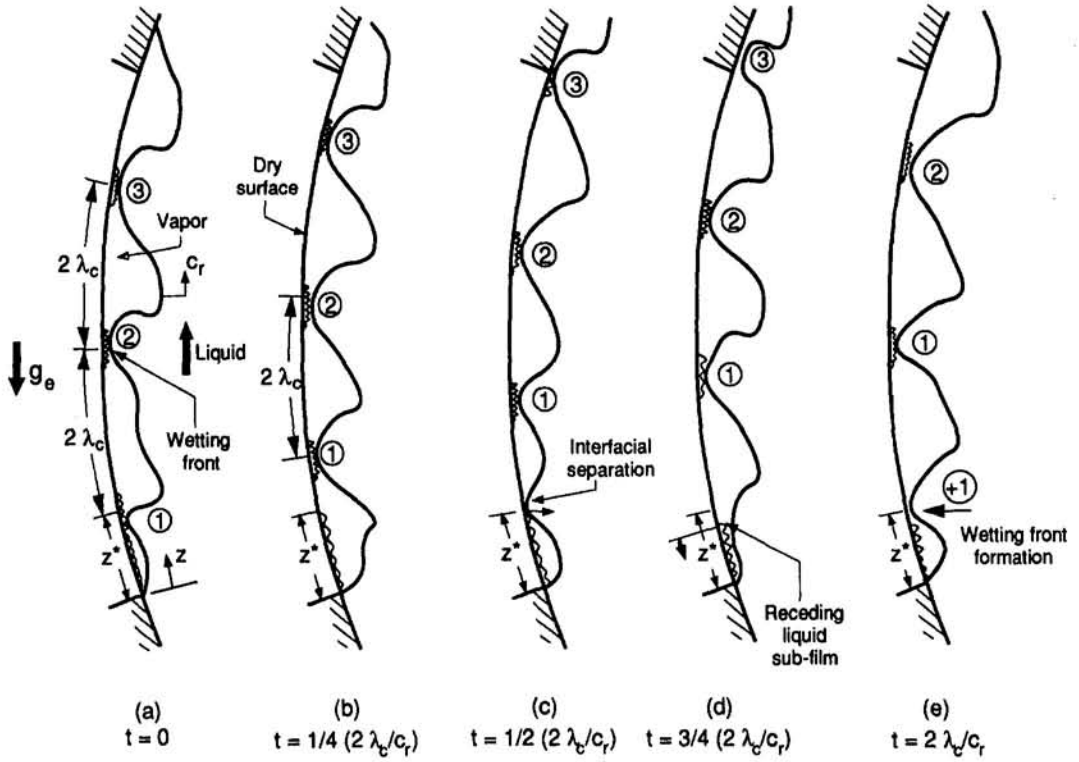

Fig. 7 Wetting front propagation along the heater surface at 99 percent of CHF

discussed by Galloway and Mudawar, 1993b), enabling liquid to contact the heater over a localized region. A short time later, at $t = \lambda_c/c_r$, another disturbance approaching the heater surface will be forced away by the momentum of vapor emanating from residual liquid at $z = z^*$ left after the passage of the previous wetting front. Not until a later time $t = 2\lambda_c/c_r$, after the residual liquid has been consumed at the location of the first wetting front, will a new wetting front be established on the heater surface. Wetting is, therefore, skipped every other cycle and wetting fronts are separated by $2\lambda_c$ wavelengths.

A Lagrangian frame of reference is used to model heat transfer to the moving wetting fronts illustrated in Fig. 7. Equation (5) sums the transient energy removed from the heater by the passage of all wetting fronts in contact with the heater between the time a wetting front first forms on the heater surface and the time the next wetting front is established at the same location. Equation (5) also accounts for the steady heat removal from the continuous wetting zone, $0 < z < z^*$.

$$q_m = \frac{c_r/(2\lambda_c)}{L - z^*}\left[\int_0^\tau\int_{z^*}^L q_{s,1}\,dz\,dt + \int_0^\tau\int_{z^*}^L q_{s,2}\,dz\,dt + \cdots + \int_0^\tau\int_{z^*}^L q_{s,n-1}\,dz\,dt + \int_0^\tau\int_{z^*}^L q_{s,n}\,dz\,dt\right] \quad (5)$$

where $q_{s,1}, q_{s,2}, \ldots, q_{s,n}$ are the local heat fluxes corresponding to wetting fronts 1, 2, ..., n, respectively. Where a wetting front is present, q_s is equal to some localized heat flux value, q_l, otherwise q_s is zero where the heater surface is dry.

The general form of Eq. (5) is identical to that derived by the authors for a short straight heater and, as illustrated in Fig. 7, gives CHF values approximately one-fourth the heat flux in the wetting fronts. Equation (5) can be simplified to the CHF expression given in Eq. (1) (see Galloway and Mudawar, 1993b).

A balance between the net pressure force exerted upon the liquid–vapor interface and the opposing momentum flux of vapor produced in the upstream wetting fronts yields an equation for the curved heater identical to that of the straight heater, Eq. (2), the difference between the two heaters being only the increased lift-off heat flux due to a greater interfacial pressure force for the curved heater as compared to the straight heater.

Combining Eqs. (1) and (2) yields an expression for CHF that is applicable to both straight and curved heaters.

$$q_m = \frac{1}{4}\rho_g h_{fg}\left(1 - \frac{\lambda_c}{16(L - z^*)}\right)\left(1 + \frac{c_{p,f}\Delta T_{sub}}{h_{fg}}\right) \times \left[\frac{\overline{P_f - P_g}}{\rho_g}\right]^{1/2} \quad (6)$$

Equation (6) shows predicting CHF requires estimation of $\overline{P_f - P_g}$. The next section will discuss an instability model, which shall be used to predict this key parameter for curved heaters.

Interfacial Instability of a Curved Vapor–Liquid Interface. The wavy vapor layer depicted in Fig. 5 clearly exhibits behavior characteristic of interfacial instability. A linearized stability analysis is proposed to model the waviness for a curved interface. While existing interfacial instability theories (Lamb, 1945; Milne-Thompson, 1960) are well suited for straight channels, these theories cannot be employed with curved flow since they do not account for the effect of radial pressurization induced by curvature; hence the need for a model specifically tailored to curved flow.

Figure 8 illustrates a wavy interface of the form $\eta = \eta_0 e^{ik(\theta R_0 - ct)}$ separating a liquid layer of thickness H_f from a vapor layer of thickness H_g inside a curved channel, where η represents the displacement of the interface from a mean position $r = R_0$, k is the wave number ($= 2\pi/\lambda$), and c is the wave speed, which can have both real and imaginary components ($c = c_r + ic_i$). Invoking the assumptions of inviscid, incompressible,

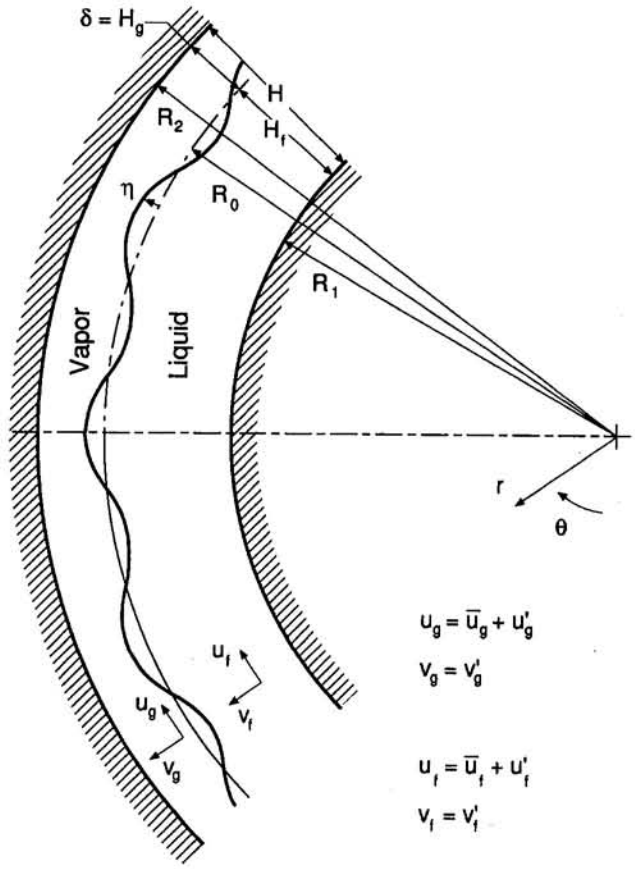

Fig. 8 Definition of hydrodynamic instability configuration and flow parameters

and irrotational flow yields the following potential function relations for liquid and vapor, respectively,

$$\nabla^2\phi_f = \frac{1}{r}\frac{\partial}{\partial r}\left(r\frac{\partial\phi_f}{\partial r}\right) + \frac{1}{r^2}\frac{\partial^2\phi_f}{\partial\theta^2} = 0, \tag{7a}$$

$$\nabla^2\phi_g = \frac{1}{r}\frac{\partial}{\partial r}\left(r\frac{\partial\phi_g}{\partial r}\right) + \frac{1}{r^2}\frac{\partial^2\phi_g}{\partial\theta^2} = 0. \tag{7b}$$

The velocity in each layer can be decomposed into a mean component in the θ direction and fluctuating components in the θ and r directions:

$$\frac{1}{r}\frac{\partial\phi_f}{\partial\theta} = u_f = \bar{u}_f + u'_f, \tag{8a}$$

$$\frac{\partial\phi_f}{\partial r} = v_f = v'_f, \tag{8b}$$

$$\frac{1}{r}\frac{\partial\phi_g}{\partial\theta} = u_g = \bar{u}_g + u'_g, \tag{9a}$$

$$\frac{\partial\phi_g}{\partial r} = v_g = v'_g. \tag{9b}$$

The solutions sought for Eqs. (7a) and (7b) are, respectively,

$$\phi_f = \bar{u}_f r\theta + F(r)e^{ik(\theta R_0 - ct)}, \tag{10a}$$

$$\phi_g = \bar{u}_g r\theta + G(r)e^{ik(\theta R_0 - ct)}, \tag{10b}$$

since, for the irrotational flow illustrated in Fig. 8, the mean tangential velocity is inversely proportional to r, $\bar{u}_f = A_f/r$, and $\bar{u}_g = A_g/r$. Equations (10a) and (10b) can be combined with Eqs. (7a) and (7b), respectively, giving

$$\frac{d^2F}{dr^2} + \frac{1}{r}\frac{dF}{dr} - \frac{(kR_0)^2}{r^2}F = 0, \tag{11a}$$

$$\frac{d^2G}{dr^2} + \frac{1}{r}\frac{dG}{dr} - \frac{(kR_0)^2}{r^2}G = 0. \tag{11b}$$

The general solutions for these equations are, respectively,

$$F(r) = a_1 r^{kR_0} + a_2 r^{-kR_0}, \tag{12a}$$

$$G(r) = b_1 r^{kR_0} + b_2 r^{-kR_0}. \tag{12b}$$

The coefficients a_1, a_2, b_1, and b_2 can be determined by applying the boundary conditions corresponding to the inner and outer solid walls and the kinematic conditions at the interface. The boundary conditions for the solid walls give $v_f]_{r=R_1} = \partial\phi_f/\partial r]_{r=R_1} = 0$ and $v_g]_{r=R_2} = \partial\phi_g/\partial r]_{r=R_2} = 0$ and, assuming particles at the interface move with the interface, these particles must satisfy the kinematic condition

$$\frac{D}{Dt}[(r - R_0) - \eta] = 0. \tag{13}$$

Equation (13) gives the following kinematic relations for the interface ($r = R_0$):

$$\frac{\partial\phi_f}{\partial r} = v_f = \frac{\partial\eta}{\partial t} + \frac{1}{r}\bar{u}_{f,i}\frac{\partial\eta}{\partial\theta}, \tag{14a}$$

$$\frac{\partial\phi_g}{\partial r} = v_g = \frac{\partial\eta}{\partial t} + \frac{1}{r}\bar{u}_{g,i}\frac{\partial\eta}{\partial\theta}. \tag{14b}$$

Combining both the boundary conditions corresponding to the solid walls and the interfacial kinematic conditions with Eqs. (6), (10a), and (12a) for the liquid layer, and Eqs. (6), (10b), and (12b) for the vapor layer gives, respectively,

$$\phi_f = A_f\theta + i(\bar{u}_{f,i} - c)\left[\frac{\left(\frac{r}{R_1}\right)^{kR_0} + \left(\frac{R_1}{r}\right)^{kR_0}}{\left(\frac{R_0}{R_1}\right)^{kR_0} - \left(\frac{R_1}{R_0}\right)^{kR_0}}\right]\eta, \tag{15a}$$

$$\phi_g = A_g\theta - i(\bar{u}_{g,i} - c)\left[\frac{\left(\frac{r}{R_2}\right)^{kR_0} + \left(\frac{R_2}{r}\right)^{kR_0}}{\left(\frac{R_2}{R_0}\right)^{kR_0} - \left(\frac{R_0}{R_2}\right)^{kR_0}}\right]\eta, \tag{15b}$$

Combining the Bernoulli equation for each phase with the mechanical equilibrium condition along the interface yields, for $r = R_0$,

$$P_f - P_g = \left[\frac{1}{2}\rho_g u_g^2 + \rho_g\frac{\partial\phi_g}{\partial t}\right] - \left[\frac{1}{2}\rho_f u_f^2 + \rho_f\frac{\partial\phi_f}{\partial t}\right]$$

$$= -\sigma\frac{\partial^2\eta}{\partial(R_0\theta)^2}. \tag{16}$$

Equation (16) can be reduced to give an expression for the pressure force exerted upon the interface:

$$P_f - P_g = [\rho_f'''(c - \bar{u}_{f,i})^2 + \rho_g'''(\bar{u}_{g,i} - c)^2]k\eta = \sigma k^2\eta, \tag{17}$$

where

$$\rho_f''' \equiv \rho_f \left[\frac{\left(\frac{R_0}{R_1}\right)^{2kR_0} + 1}{\left(\frac{R_0}{R_1}\right)^{2kR_0} - 1} \right], \quad (18a)$$

$$\rho_g''' \equiv \rho_g \left[\frac{\left(\frac{R_0}{R_2}\right)^{2kR_0} + 1}{1 - \left(\frac{R_0}{R_2}\right)^{2kR_0}} \right]. \quad (18b)$$

Solving Eq. (17) yields the following expression for c:

$$c = \frac{\rho_f''' \bar{u}_{f,i} + \rho_g''' \bar{u}_{g,i}}{\rho_f''' + \rho_g'''} \pm \sqrt{\frac{\sigma k}{\rho_f''' + \rho_g'''} - \frac{\rho_f''' \rho_g'''(\bar{u}_{g,i} - \bar{u}_{f,i})^2}{(\rho_f''' + \rho_g''')^2}}. \quad (19)$$

When the argument of the radical in Eq. (19) is negative, c acquires both real and imaginary components. In this case, $\eta = \eta_0 e^{kc_i t} \cos(k(R_0\theta - ct))$, and any interfacial perturbation becomes unstable and grows with time. Neutral stability occurs when $c_i = 0$. Setting the argument of the radical in Eq. (19) equal to zero gives

$$\lambda_c = \frac{2\pi}{k_c} = \frac{2\pi(\rho_f''' + \rho_g''')\sigma}{\rho_f''' \rho_g'''(\bar{u}_{g,i} - \bar{u}_{f,i})^2}. \quad (20)$$

Equations (17), (19), and (20) are presented here in forms that resemble those for a straight channel. The major differences between the two cases are the radial changes in phase velocities and pressure, which are manifested in the velocity terms, $\bar{u}_{f,i}$ and $\bar{u}_{g,i}$, and the new modified density terms, ρ_f''' and ρ_g'''.

CHF Model Predictions. The separated flow model given in the appendix was employed to predict local mean values of vapor layer thickness and velocities of the liquid and vapor layers in terms of inlet velocity, subcooling, and heat flux. These local values are required in order to predict the interfacial wavelength and $\overline{P_f - P_g}$.

CHF was predicted by following an iterative numerical procedure starting with a guessed value for q_m. First, this value is used in the separated flow model to determine the key parameters for the instability analysis. By discretizing z into 0.1 mm steps, an initial value for the vapor layer thickness, δ, is assumed and the interfacial vapor velocity, $\bar{u}_{g,i}$, is determined using Eq. (A.7) (since $\bar{u}_{g,i} = \bar{u}_{g,m}$), while the interfacial liquid velocity, $\bar{u}_{f,i}$, is calculated by combining Eqs. (A.5) and (A.8). The value of δ is then adjusted until the pressure calculated from the vapor layer momentum balance, Eq. (A.1), equals the interfacial liquid pressure, Eq. (A.3). The corresponding convergent values of δ, $\bar{u}_{g,i}$, and $\bar{u}_{f,i}$ are then used to calculate the critical wavelength, λ_c, using Eq. (20). The interfacial pressure difference, Eq. (17), is then averaged over the length of the most upstream wetting front, $0.25\lambda_c$, centered about the location $z = z^*$. Next, a new value for q_m is calculated using Eq. (6). In the second iteration, this newly obtained CHF value is applied through the same numerical procedure. Typically, the solution converged in less than five iterations.

Figure 9 shows that the CHF model predicts the experimental data for the straight heater (using the instability and separated flow models for a straight channel) and the curved heater with mean absolute errors of 7 and 14 percent, respectively. Some departure of the model predictions from the curved heater data at the higher end of the tested velocity range can be attributed to vapor slug detachment from wave peaks as depicted in Fig. 5, which is not accounted for in the present model. The accuracy of the model predictions is proof of the validity of both the new curved heater instability model and the assumptions used in constructing the surface energy balance and lift-off criterion. The CHF enhancement obtained with the curved heater over the straight heater is, therefore, a direct consequence of the increased curvature of the individual interfacial waves causing an increase in the net pressure force exerted upon the interface in the wetting fronts.

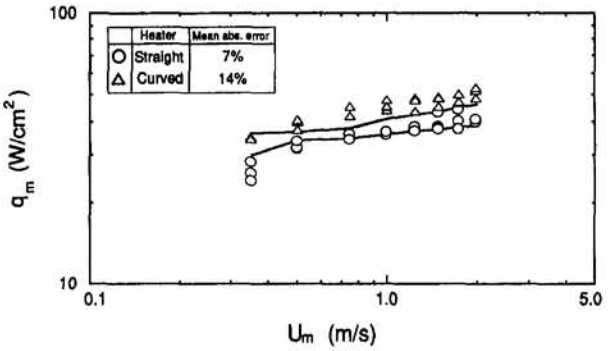

Fig. 9 Comparison of the model predictions and CHF data for the straight and curved heaters

As for the limitations of the present model, several conditions exist for which the assumptions of the model may not be valid. They include (*a*) near-critical pressure, (*b*) highly subcooled flow, where the vapor layer development may be strongly influenced by condensation along the vapor–liquid interface, (*c*) high inlet velocities corresponding to $g_n = U_m^2/R_2 > 10\ g_e$, where vapor slugs begin to detach from peaks in the wavy vapor–liquid interface, and (*d*) long heaters. A recent study by one of the authors (Gersey and Mudawar, 1995) explored the streamwise changes in the interfacial features at CHF over long heaters. The vapor waves between wetting fronts maintained equal wavelength over an axial distance close to the length of the heater used in the present study, but were found to grow downstream due to merging of adjacent waves. This behavior increased the distance between wetting fronts, resulting in smaller CHF for long heaters as compared with heaters close in size to the one used in the present study. These findings, while determined from straight heater experiments, clearly indicate the present model should not be applied to long straight or curved heaters.

6 Summary

Experiments were performed with both straight and curved heaters to ascertain the effect of streamwise curvature on CHF. Key conclusions from the study are as follows:

1 A fairly continuous wavy vapor layer was observed to engulf the heater surface at heat fluxes smaller than CHF with both the straight and curved heaters. Boiling was still active in wetting fronts where the interface of the vapor layer made contact with the heater surface. CHF was triggered when the normal momentum of the vapor produced in the wetting front exceeded the pressure force exerted upon the interface due to interfacial curvature.

2 At high velocities, the curvature caused vapor slugs to detach from peaks in the wavy vapor–liquid interface normal to, and away from the surface. No such behavior was observed with the straight heater.

3 Higher CHF was both measured and predicted for the curved heater, using a new instability model for curved flow, than for the straight heater due to the increased pressure resistance to interfacial separation in the case of the curved heater.

CHF data were predicted for the straight and curved heaters with mean absolute errors of 7 and 14 percent, respectively.

Acknowledgments

The authors are grateful for the support of the Office of Basic Energy Sciences of the U.S. Department of Energy (Grant No. DE-FE02-93ER14394). The authors also thank the Industrial Chemical Products Division of 3M Company for donating samples of Fluorinert FC-87 for the present study.

References

Costello, C. P., and Adams, J. M., 1963, "Burnout Heat Fluxes in Pool Boiling at High Accelerations," *Proc. 2nd Int. Heat Transfer Conf.,* Boulder, CO, pp. 255–261.

Fiori, M. P., and Bergles, A. E., 1970, "Model of Critical Heat Flux in Subcooled Flow Boiling," *Proc. 4th Int. Heat Transfer Conference,* Vol. 6, Versailles, France, pp. 354–355.

Galloway, J. E., and Mudawar, I., 1989, "Boiling Heat Transfer From a Simulated Microelectronic Heat Source to a Dielectric Liquid Film Driven by a Rotating Stirrer," *Heat Transfer in Electronics,* ASME HTD-Vol. 111, pp. 66–77.

Galloway, J. E., 1991, "Critical Heat Flux Enhancement in the Presence of Stream-wise Curvature," Ph.D. Thesis, School of Mechanical Engineering, Purdue University, West Lafayette, IN.

Galloway, J. E., and Mudawar, I., 1992, "Critical Heat Flux Enhancement by Means of Liquid Subcooling and Centrifugal Force Induced by Flow Curvature," *Int. J. Heat Mass Transfer,* Vol. 35, pp. 1247–1260.

Galloway, J. E., and Mudawar, I., 1993a, "CHF Mechanism in Flow Boiling From a Short Heated Wall—Part 1. Examination of Near-Wall Conditions With the aid of Photomicrography and High-Speed Video Imaging," *Int. J. Heat Mass Transfer,* Vol. 36, pp. 2511–2526.

Galloway, J. E., and Mudawar, I., 1993b, "CHF Mechanism in Flow Boiling From a Short Heated Wall—Part 2. Theoretical CHF Model," *Int. J. Heat Mass Transfer,* Vol. 36, pp. 2529–2540.

Gambill, W. R., and Green, N. D., 1958, "Boiling Burnout With Water in Vortex Flow," *Chem. Eng. Prog.,* Vol. 54, pp. 93–102.

Gersey, C. O., 1993, "Effects of Orientation and Heater Length on Critical Heat Flux From Discrete and Continuous Heaters," Ph.D. Thesis, School of Mechanical Engineering, Purdue University, West Lafayette, IN.

Gersey, C. O., and Mudawar, I., 1995, "Effects of Heater Length and Orientation on the Trigger Mechanism for Near-Saturated Boiling CHF—Part 1. Photographic and Statistical Characterization of the Near-Wall Interfacial Features," *Int. J. Heat Mass Transfer,* Vol. 38, pp. 625–642.

Gu, C. B., Chow, L. C., and Beam, J. E., 1989, "Flow Boiling in a Curved Channel," in: *Heat Transfer in High Energy/High Heat Flux Applications,* R. J. Goldstein, L. C. Chow, and E. E. Anderson, eds., ASME HTD-Vol. 119, pp. 25–32.

Hino, R., and Ueda, T., 1985a, "Studies on Heat Transfer and Flow Characteristics in Subcooled Flow Boiling—Part 1. Boiling Characteristics," *Int. J. Multiphase Flow,* Vol. 11, pp. 269–281.

Hino, R., and Ueda, T., 1985b, "Studies on Heat Transfer and Flow Characteristics in Subcooled Flow Boiling—Part 2. Flow Characteristics," *Int. J. Multiphase Flow,* Vol. 11, pp. 283–297.

Hughes, T. G., and Olson, D. R., 1975, "Critical Heat Fluxes for Curved Surface During Subcooled Flow Boiling," *Trans. Canadian Soc. Mech. Eng.,* Vol. 3, pp. 122–130.

Iverson, A. H., and Whitaker, S., 1988, "Progress in the Development of a New High Heat Load X-Ray Tube," *Proc. Society of Photo-Optical Instrumentation Engineers,* Vol. 914, *Medical Imaging II,* pp. 219–230.

Lamb, H., 1945, *Hydrodynamics,* 6th ed., Dover Publications, New York, p. 371.

Marto, P. J., and Gray, V. H., 1971, "Effects of High Acceleration and Heat Fluxes on Nucleate Boiling of Water in an Axisymmetric Rotating Boiler," NASA TN D-6307.

Milne-Thompson, L. M., 1960, *Theoretical Hydrodynamics,* 4th ed., Macmillan, New York, p. 409.

Miropol'skiy, Z. L., and Pikus, V. Y., 1969, "Critical Boiling Heat Fluxes in Curved Channels," *Heat Transfer—Soviet Research,* Vol. 1, pp. 74–79.

Mishra, P., and Gupta, S. N., 1979, "Momentum Transfer in Curved Pipes, 1. Newtonian Fluids," *Ind. Eng. Chem. Process Des. Dev.,* Vol. 18, pp. 130–137.

Mudawar, I., 1986, "Interfacial Instabilities of Air-Driven Liquid Films," *Int. Comm. Heat Mass Transfer,* Vol. 13, pp. 535–543.

Usenko, V. I., and Fainzil'berg, S. N., 1974, "Effects of Acceleration on the Critical Heat Load With the Boiling of Freons on Elements Having Small Transverse Dimensions," *High Temperature,* Vol. 12, pp. 490–495.

Zuber, N., Tribus, M., and Westwater, J. M., 1961, "The Hydrodynamic Crisis in Pool Boiling of Saturated and Subcooled Liquid," *Int. Dev. in Heat Transfer,* ASME, pp. 230–236.

APPENDIX

Separated Flow Model

Variations of the local mean vapor layer thickness and mean liquid and vapor velocities with angular position θ were predicted from a separated two-phase slip flow model. This model employs different velocities for the liquid and vapor phases and, since it does not match these velocities at the interface, an appropriate friction factor is used to match the interfacial shear stresses. The wavy vapor layer depicted in Fig. 5 was approximated as a smooth vapor layer, which increases in thickness in the flow direction due to vapor production in the upstream continuous wetting zone and in the wetting fronts. The radial pressure gradient is proportional to the density of the respective medium. Since the density of vapor is much smaller than that of liquid, the radial changes across the vapor layer are negligible compared to those across the liquid layer. Therefore, both the pressure and mean tangential velocity across the vapor layer can be assumed uniform in the radial direction.

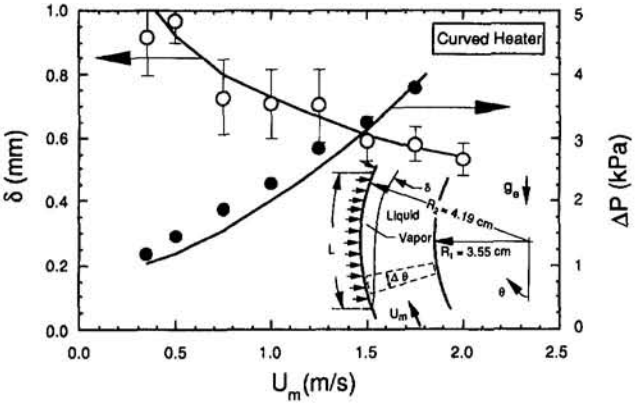

Fig. A.1 Comparison of separated flow model predictions and measurements of mean vapor layer thickness at $z/L = 2/3$ and pressure drop

Writing a momentum balance across the vapor portion of the differential control volume shown in Fig. A.1, neglecting radial changes in both vapor velocity and vapor pressure, gives

$$\rho_g \frac{d}{dz}(\bar{u}_{g,m}\delta) = \delta \frac{dP_i}{dz} - \tau_g\left(1 + \frac{2\delta}{s}\right) - \tau_i - \rho_g g_e \delta \sin(\theta), \quad \text{(A.1)}$$

where τ_g and τ_i are the wall and interfacial shear stresses, respectively, and $z = R_2\theta$.

The liquid layer thickness and liquid density are much greater than those of the vapor layer; hence, radial changes in velocity and pressure across the liquid layer cannot be ignored. Assuming the liquid flow is irrotational gives $\bar{u}_f = A_f/r$, where A_f is a function of θ only, which can be expressed in terms of the mean velocity across the liquid layer, $\bar{u}_{f,m}$, by integrating $\bar{u}_f$ from $r = R_1$ to $R_2 - \delta$:

$$A_f = \frac{\rho_f \bar{u}_{f,m}[(R_2 - \delta) - R_1]}{\int_{R_1}^{R_2-\delta} \rho_f \frac{1}{r}\, dr} = \left[\frac{(R_2 - \delta) - R_1}{\ln\left(\frac{R_2 - \delta}{R_1}\right)}\right] \bar{u}_{f,m}. \quad \text{(A.2)}$$

Integrating Euler's equation for the liquid, $dP_f/dr = \rho_f \bar{u}_f^2/r$, between any arbitrary radius r and the vapor–liquid

interface, $R_2 - \delta$, gives

$$P_f = P_i - \frac{1}{2}\rho_f \left[\frac{(R_2 - \delta) - R_1}{\ln\left(\frac{R_2 - \delta}{R_1}\right)}\right]^2 \left[\frac{1}{r^2} - \frac{1}{(R_2 - \delta)^2}\right] \bar{u}_{f,m}^2. \quad (A.3)$$

A momentum balance (per unit channel width) for the control volume shown in Fig. A.1 gives

$$\frac{d}{d\theta}(\rho_g \bar{u}_{g,m}^2 \delta) + \frac{d}{d\theta}\left[\int_{R_1}^{R_2-\delta} \rho_f \bar{u}_f^2 dr\right] = -\frac{d(P_i\delta)}{d\theta} - \frac{d}{d\theta}\left[\int_{R_1}^{R_2-\delta} P_f dr\right] - \tau_g\left[R_2 + \frac{2R_2\delta}{s}\right] - \tau_f\left[R_1 + \frac{1}{s}((R_2 - \delta)^2 - R_1^2)\right] - \rho_g R_2 \delta g_e \sin(\theta) - \rho_f\left[\frac{(R_2 - \delta)^2 - R_1^2}{2}\right] g_e \sin(\theta). \quad (A.4)$$

The shear stresses in Eqs. (A.1) and (A.4) are defined, respectively, as $\tau_g = 0.5 f_g \rho_g \bar{u}_{g,m}^2$, $\tau_f = 0.5 f_f \rho_f \bar{u}_{f,m}^2$, and $\tau_i = 0.5 f_i \rho_g (\bar{u}_{g,m}^2 - \bar{u}_{f,i}^2)^2$, where, from Eq. (A.2),

$$\bar{u}_{f,i} = \left[\frac{(R_2 - \delta) - R_1}{\ln\left(\frac{R_2 - \delta}{R_1}\right)}\right] \frac{\bar{u}_{f,m}}{R_2 - \delta}. \quad (A.5)$$

The wall friction factors f_f and f_g were determined from the following curved channel flow correlation (Mishra and Gupta, 1979):

$$f = \frac{0.079}{\mathrm{Re}^{0.25}} + 0.0075\left(\frac{D_h}{2R_2}\right)^{0.5}, \quad (A.6)$$

where Re was based on the hydraulic diameter, D_h, for the liquid or vapor layer cross section and respective mean velocity. For infinite values of R_2 (straight heater), Eq. (A.6) reduces to the Blasius equation for turbulent channel flow.

An approximate range for the interfacial friction factor, f_i, was determined from a study of air flow over solid waves (Mudawar, 1986) having features resembling those observed in the present study. A constant value of 0.5 provided the best agreement between measured and predicted pressure drop and mean vapor layer thickness in the study of CHF over a straight heater (Galloway and Mudawar, 1993b). Gersey (1993) validated the accuracy of setting $f_i = 0.5$ by examining numerous correlations in the two-phase literature for wavy vapor–liquid interfaces. The same value was used in the present study for predicting the curved channel flow parameters.

The momentum Eqs. (A.1) and (A.4) yield two differential equations relating P_i, δ, $\bar{u}_{g,m}$, and $\bar{u}_{f,m}$. Two additional differential equations can be written using mass conservation for the vapor and liquid layers, respectively:

$$\bar{u}_{g,m} = \frac{q_m z}{\rho_g \delta (c_{p,f}\Delta T_{\mathrm{sub}} + h_{fg})}. \quad (A.7)$$

$$\bar{u}_{f,m} = \frac{U_m(R_2 - R_1)}{(R_2 - \delta) - R_1} - \frac{q_m z}{\rho_f((R_2 - \delta) - R_1)(c_{p,f}\Delta T_{\mathrm{sub}} + h_{fg})}. \quad (A.8)$$

Figure A.1 shows that the separated flow model gives excellent predictions of both pressure drop and mean vapor layer thickness at heat fluxes approaching CHF. These results validate the accuracy of the separated flow model independent from the other submodels presented in this paper for predicting CHF. The pressure drop data were measured with an uncertainty of 0.1 kPa.

The key parameters required in the curved heater instability model are δ, $\bar{u}_{f,i}$, and $\bar{u}_{g,i}$. Knowing $\bar{u}_{f,m}$, Eq. (A.5) can be used to determine $\bar{u}_{f,i}$, and, because of the small density of vapor, $\bar{u}_{g,i} = \bar{u}_{g,m}$.